

# Chapter 12

## CEA–CERN Block-Type Dipole Magnet for Cable Testing: FRESCA2



Etienne Rochepault and Paolo Ferracin

**Abstract** The FRESCA2 dipole magnet, with a nominal field of 13 T in a 100 mm aperture, has been developed within a collaboration between the Commissariat à l’Energie Atomique et aux Energies Alternatives (CEA) and the European Organization for Nuclear Research (CERN), in the framework of the European Coordination for Accelerator Research and Development (EuCARD) project. This chapter summarizes magnet design, technology development, fabrication, and test results.

### 12.1 Introduction

In 2009, the European Coordination for Accelerator Research and Development (EuCARD) project was initiated, with the goal of carrying out research on new concepts and technologies for future upgrades of European accelerators (de Rijk 2012). Work Package 7 was dedicated to superconducting high-field magnets towards higher luminosities and energies. Key partners were the Commissariat à l’Energie Atomique et aux Energies Alternatives (CEA), Saclay, and the European Organization for Nuclear Research (CERN). The main objective of the work package was the design, fabrication, and test of the Facility for the REception of Superconducting CABLEs (FRESCA2), a 100 mm aperture dipole generating a nominal bore field of 13 T and an ultimate field of 15 T, aiming at providing a new facility to test superconducting cables at CERN in high magnetic fields.

---

E. Rochepault (✉)

CEA Paris-Saclay (Commissariat à l’énergie atomique et aux énergies alternatives Paris-Saclay), Saclay, France

e-mail: [Etienne.Rochepault@cea.fr](mailto:Etienne.Rochepault@cea.fr)

P. Ferracin

CERN (European Organization for Nuclear Research) Meyrin, Genève, Switzerland

e-mail: [Paolo.Ferracin@cern.ch](mailto:Paolo.Ferracin@cern.ch)

© The Author(s) 2019

D. Schoerling, A. V. Zlobin (eds.), *Nb<sub>3</sub>Sn Accelerator Magnets*, Particle Acceleration and Detection, [https://doi.org/10.1007/978-3-030-16118-7\\_12](https://doi.org/10.1007/978-3-030-16118-7_12)

311

**Table 12.1** Comparison of FRESKA and FRESKA2

Parameter	FRESKA	FRESKA2
Superconductor	Nb-Ti	Nb <sub>3</sub> Sn
Nominal bore field (T)	9.5	13
Short sample bore field at 1.9K (T)	10	17.5
Free bore aperture (mm)	88	100
Short sample current at 1.9 K (kA)	13.6	14.9
Stored energy at short sample (MJ/m)	0.7	5.5
Lorentz force $F_x$ /quadrant at $I_{nom}$ (MN/m)	3.7	7.7
Good field length at 1% (mm)	600	540
Total length (mm)	1700	2200
Outer diameter (mm)	740	1030
Mass (t)	7.8	8.8

From 2009–2013 the work was performed in the framework of EuCARD; after 2014 the project continued in the framework of a collaborative contract between CEA and CERN. The fabrication of the Nb<sub>3</sub>Sn coils started in the spring of 2015 at CEA. CEA wound the coils and CERN carried out their heat treatment and impregnation. After finalizing the first four coils, magnet assembly was carried out at CERN in early 2017. The subsequent test campaigns took place at CERN. During the first test run a faulty coil was detected. It was exchanged, and the magnet was retested. This second assembly, called FRESKA2b, exceeded the nominal target and reached a bore field of 13.3 T. A third assembly, FRESKA2c, with increased pre-stress, was tested in the spring of 2018 and reached a maximum bore field of 14.6 T at 1.9 K, setting a new field record for dipole magnets with a usable aperture. FRESKA2 will therefore increase the available field of the dipole test station at CERN from around 10 T for FRESKA (Leroy et al. 2000) to around 14 T. FRESKA2, with high temperature superconductor (HTS) inserts generating up to 5 T (Durante et al. 2018; Lorin et al. 2016; van Nugteren et al. 2018), will make accessible a field range approaching 20 T. Table 12.1 compares the main parameters of the FRESKA and FRESKA2 magnets.

The first ideas towards such a Nb<sub>3</sub>Sn dipole magnet accessing the 14–15 T field range with an aperture in the order of 100 mm date back to the Next European Dipole (NED) program, which was launched in 2004 within the Coordinated Accelerator Research in Europe (CARE) project (Devred et al. 2006). In this program the focus was put on Nb<sub>3</sub>Sn conductor development, aiming at a critical current density ( $J_c$ ) of 1500 A/mm<sup>2</sup> at 4.2 K and 15 T, but also initially included the detailed design and fabrication of a Nb<sub>3</sub>Sn model magnet. Due to a lack of resources in this program the scope of the program was realigned to concentrate on conductor development, and the magnet design was stopped. The powder-in-tube (PIT) conductor developed in this program was used for the fabrication of some coils for FRESKA2.

## 12.2 Magnet Design

### 12.2.1 Initial Choices

The design relies on rectangular block coils with flared ends (see Figs. 12.1 and 12.2), which was inspired by HD2 and HD3 (see Chap. 11 of this book), following a concept proposed in the framework of the Superconducting Super Collider (SSC) studies (Taylor et al. 1985). After a comparison between cos-theta and block-coil layouts at the beginning of the project (Devaux-Bruchon et al. 2010), the block-coil has been chosen for the following reasons:

1. Less cable degradation due to keystoneing.
2. Easier winding: the cable only has to withstand a hard-way bend in the flared section, and no twist. The coil ends do not require end-spacers.
3. Easier assembly: the block-coils provide flat faces that are easier to align and place into contact during coil-pack assembly.
4. Easier stress management: the cables are arranged perpendicular to the main dipole force ( $x$  direction), and the structure provides the pre-stress in the same direction. The accumulation of Lorentz forces is in the outer turns, where the field is lower.

The coils are made of double-pancakes (two layers) with a layer jump in the central post. Each of the four double-pancakes is individually wound, reacted, and instrumented. The coils are impregnated with epoxy resin, together with their respective components. A magnet assembly is made up of a total of four coils: two coils 1–2 (layers 1 and 2, coil ID starting with ‘12’), and two coils 3–4 (layers 3 and 4, coil ID starting with ‘34’). The posts of coils 1–2 are made of titanium for mechanical strength; the posts of coils 3–4 are made of iron to reinforce the magnetic field in the aperture. The coil layout is optimized to obtain a field homogeneity of <1% within a diameter of two-thirds of the 100 mm aperture.

The support structure follows a shell-based concept. The lateral preload is provided by an external aluminum shell, transferred via two yoke halves and vertical and horizontal pads surrounding the coils, as shown in Fig. 12.2a. The lateral preload is tuned at room temperature using bladders and keys, and then additional preload is applied by the aluminum shell thanks to differential contraction during cool-down. The gap between the two yoke halves is left free during the cool-down to allow for the contraction of the shell.

The longitudinal preload is applied first at room temperature by pre-tensioning the Al rods connecting the two end plates, then during cool-down by differential contraction of the Al rods. A conceptual and detailed magnet design is provided by Manil (2013).

### 12.2.2 Strand and Cable Parameters

For the magnetic design a Nb<sub>3</sub>Sn strand with a non-Cu critical current density of up to 2500 A/mm<sup>2</sup> at 12 T and 4.2 K, and 1500 A/mm<sup>2</sup> at 15 T and 4.2 K (Bordini et al.

**Fig. 12.1** FRESCA2 magnet structure (longitudinal section)

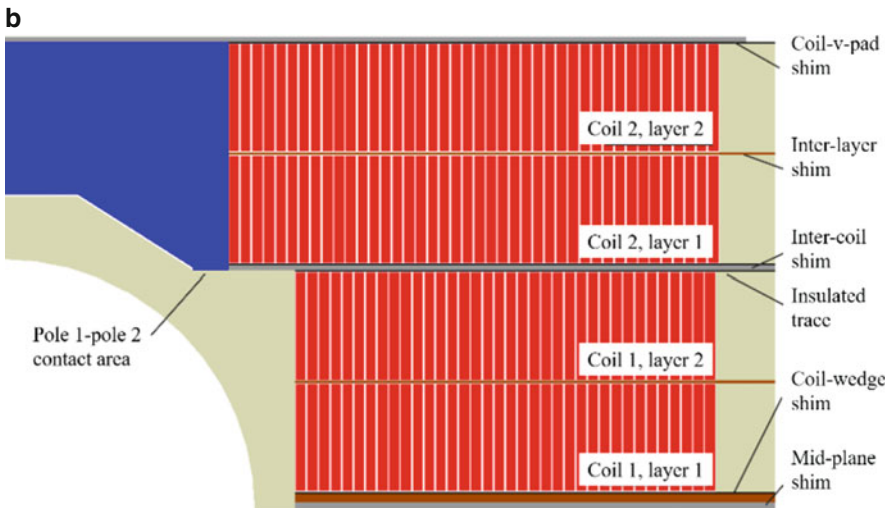
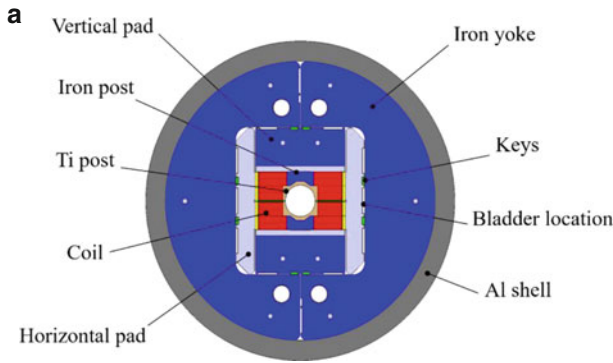
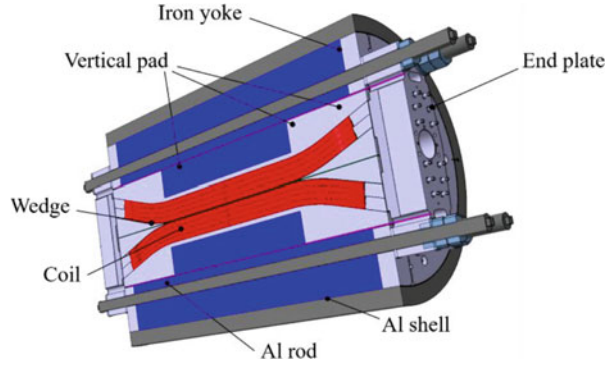


**Fig. 12.2** FRESCA2 magnet. (a) Cross-section; (b) close-up showing the coil cross-section and insulation scheme (one quadrant at the center of the straight section)

**Table 12.2** Final strand and cable parameters

Parameter	PIT	RRP
Strand diameter (mm)	1	1
Number of filaments	192	132/169
Effective filament diameter ( $\mu\text{m}$ )	48	58
RRR (extracted)	120	84–125
Cu/non-Cu ratio	1.3	1.3
$J_c(12\text{ T}, 4.2\text{ K})^a$ ( $\text{A}/\text{mm}^2$ )	2300	3000
$J_c(15\text{ T}, 4.2\text{ K})^a$ ( $\text{A}/\text{mm}^2$ )	1300	1600
Number of strands	40	40
Transposition pitch (mm)	120	120

<sup>a</sup>With self-field correction and cabling degradation

2012) was assumed. Two different strands have been procured: a PIT strand produced by Bruker-EAS GmbH, Hanau, Germany, featuring 192 filaments; and a Restacked Rod Process (RRP) strand produced by Oxford Superconductor Technology (OST), NJ, USA, featuring a 132/169 stack. The filament sizes are 48  $\mu\text{m}$  for the PIT strands and 58  $\mu\text{m}$  for the RRP strands. A Cu/non-Cu volume ratio of 1.25 was chosen to ensure protection and a large engineering current density. Table 12.2 summarizes the final target parameters of the  $\text{Nb}_3\text{Sn}$  wires.

For FRESCA2 a large rectangular Rutherford cable without a core was chosen to minimize the inductance (and increase the current) of the magnet. Due to the resulting cable's large aspect ratio, it was a challenge to make the FRESCA2 cable mechanically flexible enough for winding ('windable') and to limit its cable critical current degradation to below 5% (Oberli 2013).

To limit the number of strands in the cable to 40 (the limit of CERN's cabling machine) a 1.25 mm diameter strand initially developed for the NED program (Devred et al. 2007) was envisioned. After cabling tests, however, the cable was considered to be too large to be windable. A strand diameter of 1.0 mm was finally selected. The initial cable transposition pitch of 160 mm was reduced to 120 mm to improve the windability of the cable. The width compaction factor of the cable was optimized to limit the strand critical current degradation during cabling to 4–5%, for both PIT and RRP strands. The average residual resistivity ratio (RRR) was measured between 84 and 125 for extracted strands. Despite this relatively low RRR, measurements on short samples have shown that the stability current in both PIT and RRP extracted strands was at least twice the operating current, which was deemed sufficient not to affect the magnet's performance (Bordini et al. 2012; Oberli 2013). Cable cross-sections are shown in Fig. 12.3. The cable is insulated with braided S2 glass yarn with a thickness of 0.160 mm with 636 sizing and 11 tex.

The thicknesses of each unit length of cable produced were measured by sampling two cable stacks. The fabrication process for these stacks is considered to be representative of the coil manufacturing process. The stacks were then measured under an average pressure of 5 MPa before and after heat treatment, with insulation, and after removing the insulation. The cable geometrical parameters are summarized in Table 12.3.

The magnetic design has been initially optimized taking into account early measurements on PIT strands, considering a 10% cabling degradation, an insulation

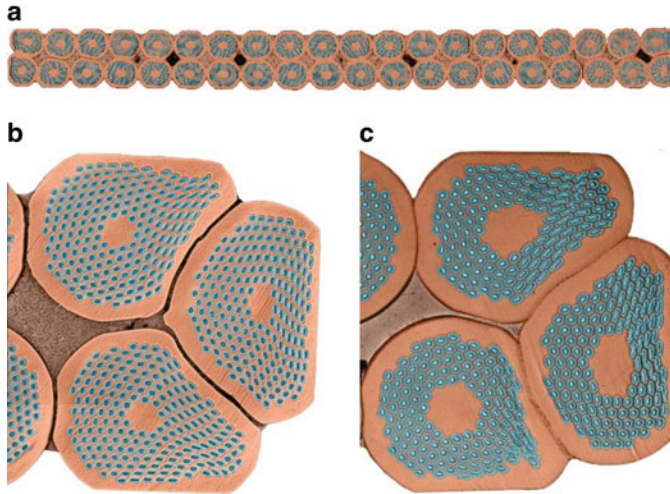


**Fig. 12.3** (a) Cross-section of a FRESCA2 cable made of 40 PIT strands of 1.0 mm diameter; and cross-section of cable edges with (b) PIT strands and (c) RRP strands

**Table 12.3** Final cable parameters

Parameter	Before reaction	After reaction
Bare thickness (mm)	1.82	1.9
Bare width (mm)	20.9	21.48
Insulation thickness (mm)	0.16	0.16
Insulated thickness (mm)	2.14	2.22
Insulated width (mm)	21.22	21.8

thickness of 0.2 mm, and not taking into account the cable expansion during reaction (Milanese et al. 2012). Later, expansions of 2% in width and 4% in thickness have been considered (Ferracin et al. 2013), corresponding to conservative assumptions with respect to measurements performed for MQXF coils (Rochepault et al. 2016). After the final determination of the expansion of the FRESCA2 cable, the tooling had already been designed and manufactured, so the insulation thickness was decreased from 0.2 mm to 0.16 mm for allowing the insertion of the coil into the tooling (Manil et al. 2014).

### 12.2.3 Magnetic Design

#### 12.2.3.1 Cross-Section Design

The rectangular block layout de facto limits the magnetic optimization to the following parameters (not considering the geometry of the iron): (a) the total number of turns; (b) the relative number of turns in coils 1–2 vs. coils 3–4; (c) the position of

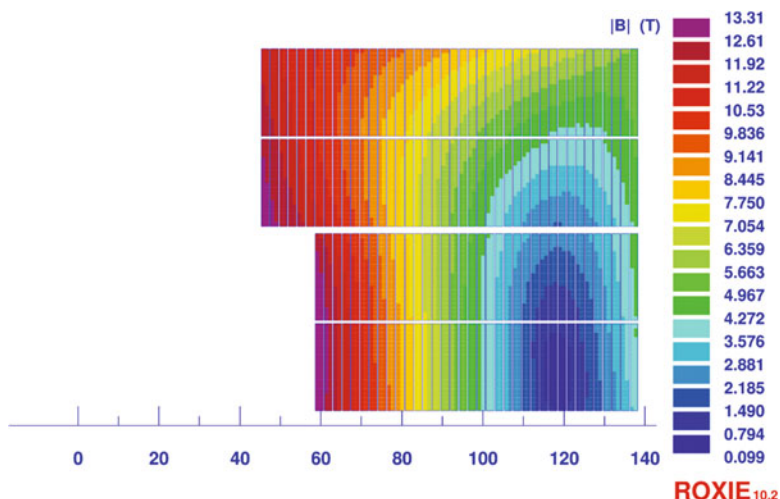


**Fig. 12.4** Baseline coil cross-section and baseline magnetic flux density in the coil (T)

the first cable in layer 1; and (d) the thickness of the mid-plane shim. The main objective was to reach 13 T nominal field with sufficient load line margin at 4.2 K ( $>10\%$ ). The required field quality was less stringent (low-order field harmonics of several tens of units) compared to accelerator magnets that are usually of the order of a few units.

The 2D magnetic optimization was performed (Milanese et al. 2012) using the ROXIE (Routine for the Optimization of magnet X-sections, Inverse field calculation and coil End design) program package. The magnetic field map and a baseline coil cross-section is shown in Fig. 12.4. The first conductor of layers 1 and 2 is placed at a distance of 58 mm from the center, whereas the mid-plane shim thickness amounts to  $2 \times 3.5 = 7$  mm. The post for coils 3–4 is made of iron, which allows an increase of the central field while reducing the coil peak field and thus increasing the margin. With all the iron parts, the nominal current for 13 T is decreased by 2 kA, and the peak field in the coil is decreased by 0.7 T.

In terms of field homogeneity, the optimization of the position of the windings resulted in a computed field quality characterized by sextupole ( $b_3$ ) and decapole ( $b_5$ ) normalized harmonics of 68.5 and  $-27.8$  units, respectively, at a reference radius of 33 mm. The saturation of the iron pole in coil 2 and in the vertical pad (see Fig. 12.2) determined a reduction of the transfer function from 2.4 T/kA at 1 kA to about 1.2 T/kA at a nominal current of 10.6 kA. The effect of magnetization has not been taken into account. A comparison between the computed and measured field quality values will be made in the section Magnetic Measurements below. The main parameters for the magnetic cross-section are summarized in Table 12.4. The nominal current, originally estimated to be 10.82 kA considering the first assumptions (Milanese et al. 2012), was re-calculated to 10.58 kA based on the updated cable parameters, the 3D magnetic finite element model (FEM), and magnetic measurements.

**Table 12.4** Main magnetic cross-section parameters

Parameter	Value
Nominal magnetic flux density (T)	13.0
Nominal current $I_{\text{nom}}$ (kA)	10.6
Number of turns in layers 1 & 2	36
Number of turns in layers 3 & 4	42
Stored energy density in straight section at $I_{\text{nom}}$ (MJ/m)	2.8
Differential inductance per unit length at $I_{\text{nom}}$ (mH/m)	41.1
Differential inductance at $I_{\text{nom}}$ (mH)	62.5
Temperature margin at $I_{\text{nom}}$ (4.2 K/1.9 K) (K)	3.0/5.3
Radius for $\Delta B/B \leq 1\%/2\%$ at $I_{\text{nom}}$ (mm)	32/42
Sextupole $b_3$ at nominal current ( $R_{\text{ref}} = 33.3$ mm)	$68.5 \times 10^{-4}$
Decapole $b_5$ at nominal current ( $R_{\text{ref}} = 33.3$ mm)	$-27.8 \times 10^{-4}$

### 12.2.3.2 3D Coil Design

To clear the aperture, flared coil ends are used (see Fig. 12.1). An inclination angle of  $17^\circ$  has been chosen after fixing the minimum distance from the mid-plane to the ends to 61 mm, to accommodate the mechanical support. This choice of inclination angle is a compromise between long planar transitions (large angles) and long inclined sections (small angles), both resulting in longer ends. The minimum hard-way bending radius of the flared ends is set to 700 mm, based on experience from HD3, for which the bending radius was increased from 349 mm to 873 mm. A short inclined section follows, with a length of 24 mm for layers 1 and 2, and 31 mm for layers 3 and 4. The coil ends follow a circular path, so the easy-way bending radius is imposed by the cross-sectional layout. Winding tests with copper cable have guided the choice of the above parameters for the end geometry. The overall coil end-to-end length is 1500 mm, whereas the minimum straight section is 730 mm. The layer jumps were placed in the ends (Fig. 12.5). The path of the layer jump was chosen to minimize the deformation of the cable.

The nominal cable length needed to wind layers 1 and 2 is 225 m, whereas 255 m are needed for layers 3 and 4. A total of about 40 km of strand (275 kg) for the overall magnet is needed.

Magnetic simulations in 3D confirm that the magnetic flux density in flared coil ends naturally decreases. The peak field can be reduced further by optimizing the geometry of the iron, and no spacers are needed in the coil ends. Contrarily, in flat racetrack coils, spacers are needed in the coil ends to reduce the magnetic flux density (Rochepault et al. 2018b). For this reason, and also considering the manufacturing aspects, the iron yoke covers the full length of the magnet, whereas the iron in the vertical pad only covers the straight section. The central post for layers 3 and 4 is a solid piece of iron. The peak flux density in the coil ends is reduced by 1.0 T with respect to the straight section, at nominal current. The magnetic length is 1.13 m, and the longitudinal 1% uniform field region has a length of 0.54 m. The total stored energy at nominal current is 3.8 MJ.

**Fig. 12.5** Layer jump (highlighted in red) between layers 3 and 4

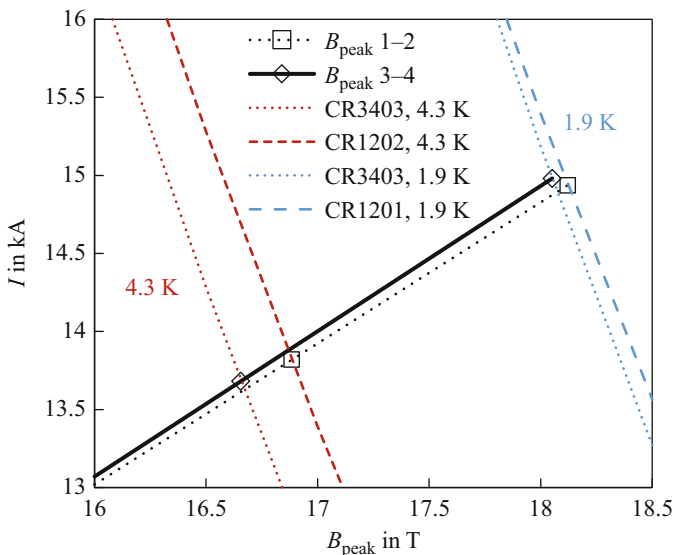
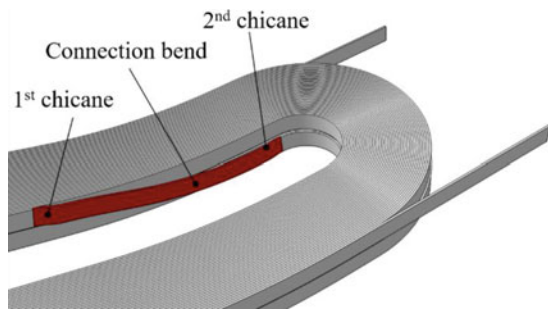


**Fig. 12.6** Load lines for coils 1–2 and 3–4 of the magnet and critical current lines at 4.3 K and 1.9 K. Self-field correction and cable degradation are considered. Short sample limits are represented only for the two coils with the lowest short sample current, and are plotted with markers

### 12.2.4 Short Sample Limits and Load Lines

The critical current is measured on virgin (round) strands and strands extracted from cables using short samples (Roche-pault et al. 2017). Measurements have been performed at 4.3 K and the data has been fitted by parameterization curves (Bordini et al. 2012) and extrapolated to 1.9 K. The degradation due to cabling, deducted from the comparison between virgin and extracted strand measurements, has been found to be on average between 2% and 5%.

Figure 12.6 illustrates the estimates for the short sample limit (SSL) current  $I_{\text{ss}}$  and peak field on the coil  $B_{\text{peak}}$  based on the computed load lines and the critical line

of extracted strands. At a nominal field of 13 T the load line margins are 23% at 4.3 K and 29% at 1.9 K. This large margin was chosen to accept a critical current degradation of up to 15%, which is comparable to HD3. For the ultimate bore field of 15 T, the load margins are 9% and 16% at 4.2 K and 1.9 K, respectively.

## 12.2.5 Mechanical Design

### 12.2.5.1 Cross-Section Design

During the first test, for each operating condition, i.e., nominal (13 T central field) and ultimate (15 T central field), the pre-stress was changed with the aim of keeping the cable compressed along the central posts, and to limit the peak stress in the coil to about 150 MPa. This choice follows the approach adapted for the HD3 dipole, and for the SMC (Perez et al. 2015) and RMC (Perez et al. 2016) racetrack models, which reached 86%, 99%, and 97% of their short sample limit, respectively. A pre-stress for the ultimate field will be applied to the magnet that will be installed in the test station.

Mechanical optimization was performed in 2D and 3D using ANSYS finite element software (ANSYS Inc., Canonsburg, PA). For the post for coils 1–2, a titanium alloy has been selected for its high yield stress and low thermal contraction. Early designs considered a removable inner tube as the interface for the magnet inserts, providing support for both the insert and the outsert. A sensitivity analysis of the tube thickness, from 6 to 10 mm, was conducted. It was considered that a value of 8 mm provided a comfortable margin for mechanical support, with a limited impact on the magnetic efficiency. The tube thickness was later included in the central post. For the lateral preload, two lateral keys per side are used in order to balance the preload forces on the coils. A thickness of 70 mm for the shell has been chosen to provide approximately 50% of the preload forces during cool-down for ultimate operation. The horizontal pad is made from stainless steel; the vertical pad is made of iron in the straight section and stainless steel in the ends. The mid-plane shim is in glass-fiber reinforced epoxy (G11).

Bonded contacts between the coils and the central posts were assumed. For all other contacts, between structural components and between the structure and the coils, separation and sliding with a friction coefficient of 0.2 was allowed. The impregnated coils are modeled as blocks with linear properties. The rigidity modulus was initially assumed to be isotropic and equal to 30 GPa and 42 GPa at 293 K and 4.2 K, respectively, with an integrated thermal contraction of 3.36 mm/m from 293 to 4.2 K (Milanese et al. 2012). Based on later mechanical measurements, the modulus was changed to 20 GPa at 293 K and 4.2 K, the friction coefficient to 0.15, and the coil thermal contraction from 293 K to 4.5 K to 3.90 mm/m.

The nominal and ultimate horizontal interference for the lateral preload is 0.6 mm and 1.1 mm, respectively. The pressure required in the bladders to open the corresponding gaps are within reach (in the order of 300–400 bar). The average

pressure between a coil and the central post, and between a coil and the horizontal pads, is positive (compression) at all operating steps. According to the model, the corresponding peak stress in the straight section, after cool-down, are 94 MPa and 109 MPa, for the two preload levels, respectively, and 95 MPa and 116 MPa for the nominal and ultimate currents, respectively (see Fig. 12.7). The estimate of the peak stress is 30–40% lower when considering the 20 GPa modulus compared to a 42 GPa modulus. Coils 3–4 are de-bonding (no contact pressure) from their central post during powering (see Fig. 12.8).

### 12.2.5.2 End Design

The coil ends are supported vertically by two stainless-steel wedges on the mid-plane (see Fig. 12.1), and the vertical pads follow the flared shape, getting progressively thinner. The coil blocks are surrounded laterally with stainless-steel rails and in the ends by stainless-steel end-shoes (reacted and impregnated with the conductor). The length of the coils including the end-shoes is 1.6 m, and is the same as the shell. The design of the end-plate takes into consideration the space needed to insert keys and bladders made of 316 L stainless steel, as well as the instrumentation wires. Its thickness has been set to 150 mm to minimize the bending stress.

## 12.2.6 Quench Simulations

A 2D electro-thermal model, implemented in CAST3M (a finite element program developed at CEA) has been used to determine the parameters of the quench protection system. Quench-back was not considered. Quench heaters are simulated on the outer surface of each layer, covering 50% of the total allowable surface, and providing 50 W/cm<sup>2</sup> (Felice et al. 2009). According to these computations, the maximum temperature  $T_{\max}$  is 125 K assuming no detection time (see Fig. 12.9). The highest temperature is in the high-field region. In order to keep  $T_{\max}$  below 200 K, the detection and circuit operation time (from quench initiation to opening of the switch and activation of the heaters) must be smaller than 100 ms. In the case of failure of two heaters out of four,  $T_{\max}$  increases by 30 K.

## 12.3 Technology Development

A series of experimental tests has been carried out prior to coil fabrication, in order to validate the technological choices made during the detailed design phase.

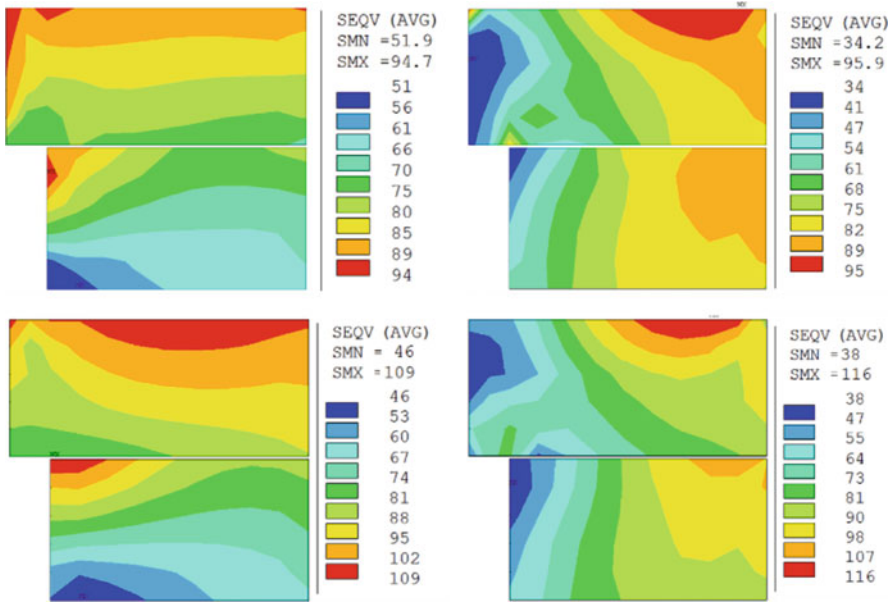


**Fig. 12.7** Coil equivalent von Mises stresses for the central sections, generated with the 3D model. Top figures: 0.6 mm preload; after cool-down (left); and powering to nominal 13 T (right). Bottom figures: 1.1 mm preload; after cool-down (left); and powering to ultimate 15 T (right)

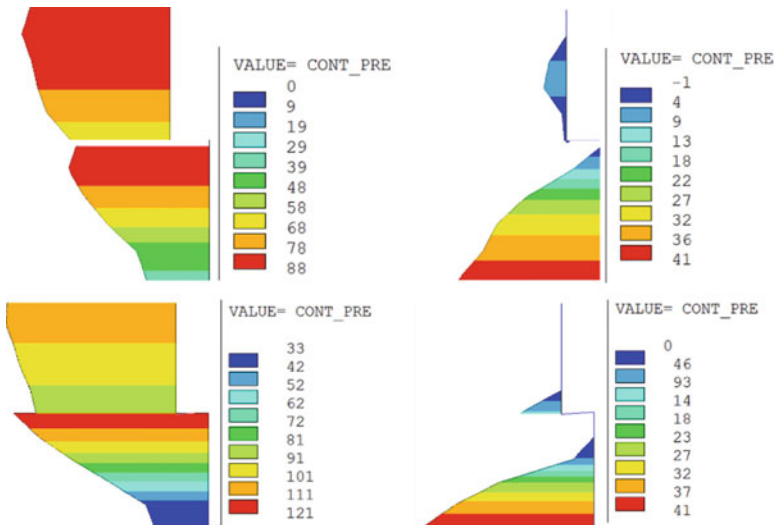
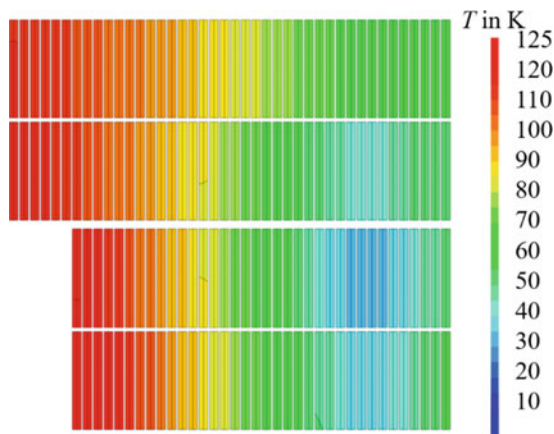


**Fig. 12.8** Coil-pole contact pressure, in MPa, for the central sections, generated with the 3D model. Top figures: 0.6 mm preload; after cool-down (left); and powering to nominal 13 T (right). Bottom figures: 1.1 mm preload; after cool-down (left); and powering to ultimate 15 T (right)

**Fig. 12.9** Temperature distribution within the dipole coil at the end of the current discharge with zero detection time



### 12.3.1 Sub-scale Winding Tests

Preliminary winding tests were first performed at CEA on a reduced mock-up (short straight section, only a few turns) using copper cables to explore and choose the winding tension, inclination angle, radius of the hard-way bend, profile of the easy-way bend, and orientation of the winding. Trials were also performed for the layer jump. These tests allowed validation of the windability of the coil ends and confirmed the choice of a block-coil layout.

### 12.3.2 Full-Scale Cu Practice Coils

The coil fabrication process and the tooling design have been tested and validated on two full-scale practice coils, 1–2 and 3–4, using copper cables. The Cu cable had a slightly larger thickness (2.24 mm compared to the nominal 2.22 mm), so only 40 turns have been wound instead of the nominal 42 turns.

### 12.3.3 Dimensional Changes During Heat Treatment

As learned from previous projects,  $\text{Nb}_3\text{Sn}$  cable sections expand and contract longitudinally during heat treatment due to stress release and the phase transition during  $\text{Nb}_3\text{Sn}$  formation. The exact changes in dimensions of the coils is difficult to predict and depends greatly on the cable and coil fabrication process. The tooling has to allow for a contraction in the longitudinal direction and an expansion in the cross-section, in order to reduce residual stress and potential degradation. To determine the exact change of dimension during heat treatment, a series of measurements was

performed on cable stacks and on sub-scale racetrack coils (short length, only a few turns) (Durante et al. 2016).

Following the observations on the sub-scale coils, the winding and reaction tooling has been split longitudinally into three sub-elements (Manil et al. 2014; Rondeaux et al. 2016) to cope with the longitudinal contraction. The tooling has been adapted so the sub-elements are able to freely move axially during the heat treatment. The central post and rails are also cut along the straight section. Each post part is fixed to one sub-element of the winding table, and the gaps between the post parts are precisely defined by using shims placed between the sub-elements. These shims are placed before winding and are removed before heat treatment.

Tests have been performed with the modified tooling described above for coils 3–4, using only four turns of conductor. The missing 38 turns have been replaced by filling blocks, leaving the same relative space for the cable to expand transversally during heat treatment. The coils were wound at CEA and heat-treated at CERN. The first test was performed with an RRP cable, assuming a longitudinal contraction of 1% (Manil et al. 2014). The gaps were distributed at the lead end (6 mm) and the return end (10 mm). In that configuration, it was expected that the gaps would not close, which would allow an in situ measurement of the coil contraction. Surprisingly, the gaps reduced by only 3.2 mm (see Table 12.5) instead of the expected 13.2 mm reduction, so a second test was performed introducing a total gap of only 3 mm, expecting that the gaps would fully close. In this configuration, however, a reduction of the gap of only 1 mm was observed. Excessive friction or stuck parts were suspected, and two additional tests were performed (using a PIT cable) in a configuration with reduced friction (removing guiding features and placing additional mica layers). Even with reduced initial gaps, however, the gaps never fully closed.

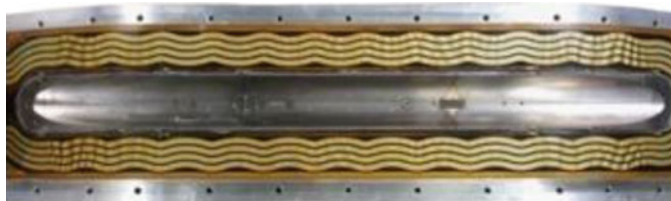
Following these tests, it was decided to place shims with a thickness of 1 mm between the blocks of the winding table before winding. After winding, the gaps were closed manually by removing the shims and putting the blocks back in contact. This approach provides an extra cable length of 0.13% inside the mold, gives a margin to release the winding tension, and allows for cable contraction during reaction. As a comparison, overall contractions of the order of  $-0.3$  to  $-0.15\%$  have been reported for MQXF coils (Rochepault et al. 2016).

### ***12.3.4 Quench Protection and Instrumentation***

The stored energy density in the coil is comparable to previously built magnets, allowing for similar protection approaches. For FRESCA2, quench protection is provided by using a dump resistor and quench heaters. The quench heater design, shown in Fig. 12.10, is based on 25  $\mu\text{m}$  thick and 12 mm wide stainless-steel strips sandwiched between polyimide films. To cover the 80 mm wide coils two nested families of heaters are installed, going from the connection side to the

**Table 12.5** Full-scale coil contractions

Coil	Initial gaps (mm)	Gap contraction (mm)	Coil contraction (%)
DR3401 (RRP)	15.7	−3.3	−0.25
DR3402 (RRP)	3.0	−1.0	−0.08
Sub-scale (insulated, fixed, Fe post, RRP)	25	−2.4 to −0.9	−0.35 to −0.15
DP3401 (PIT)	4.0	−1.6	−0.12
DP3402 (PIT)	4.0	−0.2	−0.01
Sub-scale coils (insulated, fixed, Fe post, PIT)	25	−3.2 to −1.7	−0.45 to −0.25

**Fig. 12.10** Quench heater impregnated at the surface of a coil

non-connection side and back, with a wiggling shape and without heating stations. The total integrated length of the heaters is 3.1 m (four turns), with a total surface per circuit of 370 cm<sup>2</sup>, and a total resistance of 8 Ω. The required power of 51 kW is provided with a current of 80 A and a voltage of 640 V. This quench heater technology was previously successfully applied to the RMC magnets.

## 12.4 Magnet Fabrication

### 12.4.1 Coil Fabrication

The coil fabrication process follows four main stages (Manil et al. 2014; Rondeaux et al. 2016): winding (with un-reacted cable), heat treatment, post-heat treatment operations, and impregnation with epoxy resin. Each single double-pancake is fabricated separately, with two different sets of tooling.

So far, six coils have been produced: five coils using RRP conductor (CR1201, CR1202, CR3401, CR3402, and CR3403, see Fig. 12.11) and one coil using PIT conductor (CP1203). A second PIT coil (CP3404) will be produced: the cable unit length is available and the components are being procured. A detailed description of coil fabrication is provided by Rochepault et al. (2017) and Rondeaux et al. (2016).



**Fig. 12.11** Four Nb<sub>3</sub>Sn coils of one magnet are ready for the first magnet assembly

#### 12.4.1.1 Winding

The coil winding operation was performed at CEA on a horizontal winding machine. Due to a large spring-back of the cable, a ‘swelling’ appears in the straight section. Therefore, when compressing the coils laterally with rails, the excess of conductor is transferred to the ends, and gaps open between the coil ends and the central post. Consequently, the coil ends were 1.4–4.0% thicker than nominal, the coils were 0.2–0.5% longer, and the end-shoes were outwardly misaligned by a few mm.

The winding tooling is kept for the heat treatment. All of the following operations were performed at CERN.

#### 12.4.1.2 Heat Treatment

The heat treatment cycle was optimized on short samples for a large critical current and RRR. The following heat treatment cycle for the RRP cable has been used:

- Ramp at 25 °C/h, held for 72 h at 210 °C;
- Ramp at 50 °C/h, held for 48 h at 400 °C;
- Ramp at 50 °C/h, held for 50 h at 650 °C.

Six witness samples for critical current measurements were systematically reacted with the coils.

As explained above, coils usually contract longitudinally during the heat treatment. For coils 1–2, the gaps introduced during winding remained closed, and the coils contracted globally as expected. The remaining additional length was compensated for by varying the insulation thickness between the coil and the end-shoes. Unexpectedly, however, coils 3–4 contracted very little and remained a total of 0.4–0.5% longer. Additional gaps even re-opened between the post pieces, and between the coil ends and the post. This behavior is attributed to the higher thermal

expansion of the iron posts, preventing the contraction of coils 3–4 during heat treatment. The extra length has been compensated for by re-machining the end-shoes.

After the heat treatment of CR1201 (coil with open bore), a significant deformation of the Ti post (up to 1.5 mm) was observed. This deformation was attributed to the volume expansion of the coil during reaction. The post was machined after impregnation to allow assembly. For the next coils, filler pieces were inserted into the bore during heat treatment. This technique was first applied in the HD3 coils and allowed the avoidance of any deformation.

#### **12.4.1.3 Instrumentation, Splicing, and Preparation for Impregnation**

Each layer is instrumented with traces consisting of the abovementioned quench heater circuits and connections for up to 10 voltage taps. On the outer side of the trace 0.2 mm of glass-fiber cloth was added.

The Nb<sub>3</sub>Sn leads are spliced to Nb-Ti leads and the splice is attached to the end-shoes. During the splicing of coil CR3401, some strands were accidentally damaged. The area was then repaired by soldering a copper stabilizer to provide both a mechanical support and stabilization in case of a quench.

#### **12.4.1.4 Impregnation**

The coils are impregnated inside a vacuum impregnation tank, using CTD-101K epoxy resin from Composite Technology Development (CTD), Lafayette CO, US. The pressure inside the mold is around 10 mbar before impregnation, with the autoclave being at  $10^{-3}$  mbar. Resin curing is made at atmospheric pressure, with a first step of 6 h at 110 °C, followed by 16 h at 125 °C.

Impregnation of coil CR1201 failed during the first attempt and only two-thirds of the coil volume was filled with epoxy. A second impregnation was performed by machining new injection holes into the impregnation mold.

For CR3401, some air volumes were accidentally trapped in the cavity and released during impregnation, which created some voids at the surface of the coil. The impregnation was repaired by locally re-impregnating each void. This issue is likely to be the source of the damage to the quench heaters. For the subsequent coils, adequate filler pieces were used, the sealing of the mold was improved, and no further issues were observed.

### **12.4.2 Magnet Assembly**

#### **12.4.2.1 Coils' Pairing**

Out of the first four coils produced, pairs of coils 1–2 and 3–4 were selected for the best dimensional fit. All possible combinations have been studied based on the

dimensional measurements performed after coil fabrication. The most favorable case was to pair CR1201 with CR3402 and CR1202 with CR3401, providing a minimum of 0.1 mm clearance for assembly. In the second magnet, FRESCA2b, CR3401 was replaced by the spare coil CR3403 (Bourcey et al. 2018).

The ground insulation scheme initially proposed relied on coil-to-post insulation, with contact post-to-post. The measured post-to-coil resistances were, however, lower than expected; therefore, the insulation scheme was modified by adding polyimide layers between the posts during magnet assembly.

#### 12.4.2.2 Double-Coil Assembly

In order to compensate for potential shape defects of the coils, a tailor-made shim of about 0.9 mm thickness is impregnated between coils 1–2 and coils 3–4 (Fig. 12.12). Coil 3–4 is placed on top of coil 1–2, making sure that the posts are in good contact in the straight section. The coils are then clamped and the tooling is closed and sealed to allow for vacuum impregnation with Araldite MY750 charged resin to fill the gap between the coils. A mold release agent is applied on all of the surfaces in contact with the resin so as to allow disassembly of the two coils in the case of a replacement being required.

The electrical resistance between the central posts of coils 1–2 and 3–4 was checked before and after the tailored shim impregnation by applying different voltage levels. After the impregnation of pole 2 (CR1202/CR3401), a short was detected. After disassembly, it became evident that the resin did not flow in between the central posts. The polyimide insulation was reinforced for the second attempt and the result was satisfactory (16 G $\Omega$  at 1 kV).

#### 12.4.2.3 Pole Assembly

Once the coil assembly is finalized, a vertical pad is placed on coil 3–4, with a 1 mm G10 insulating shim between. Two wheels have been designed to be able to rotate the assembly by 180°, lift, and then position it. The mid-plane insulation and the wedges are then installed to complete the half coil-pack, providing a flat mid-plane for the assembly of the second pole. Two layers of 0.125 mm thick polyimide film were added in the mid-plane and bent in the aperture to ensure electrical insulation between the Ti central posts. The same operations are repeated for the second pole. The first pole is then lifted and positioned carefully on top of the second pole (see Fig. 12.13). To do so, a lifting beam is mounted into the aperture of coil 1–2, and attached at the ends of the vertical pad. The lifting beam is finally slid out of the aperture, taking care to not damage the strain gauges and wires.



**Fig. 12.12** Coils 1–2 and 3–4 installed in the tailored shim impregnation mold

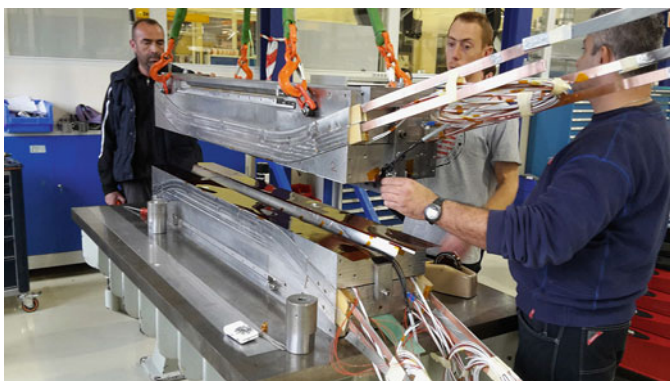


**Fig. 12.13** Manual assembly process of the two poles together using dedicated tooling

#### 12.4.2.4 Magnet Preloading

Finally, the coil-pack is centered horizontally and vertically in the structure by using the bladders and inserting the first keys (see Fig. 12.14). The axial loading system is assembled before starting the preloading operations (see Fig. 12.15).

The preload is subdivided in three loading sub-steps but, depending on the available shim sizes and the evolution of the stress, some intermediate steps may be added. The stress is monitored using strain gauges at various locations on the poles (CR1201 and CR1202) and on the shell (only the mid-plane locations S1M and S2M will be described). For the three assemblies, the post stress vs. shell stress (transfer function) was linear, as expected from the FE model. The agreement with the measurements are within a few MPa. Both FRESCA2a and FRESCA2b were loaded at room temperature until there was a stress of around 150 MPa in Ti post 1–2 and 30 MPa in the Al shell, corresponding to a peak stress in the coil of approximately 30 MPa. More details on the analysis can be found in Rochepault et al.

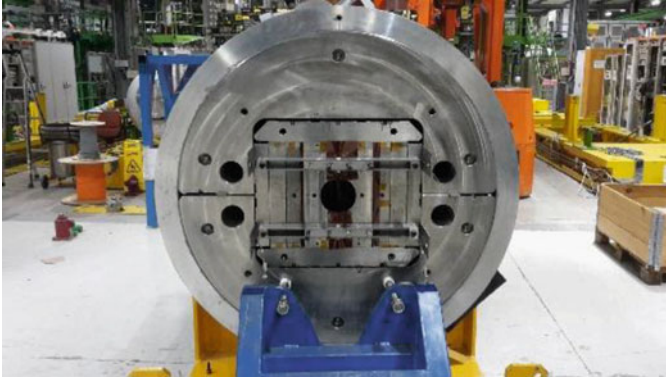


**Fig. 12.14** Magnet after coil-pack insertion. The picture shows the elements of the assembly

**Fig. 12.15** Magnet ready for preloading with axial loading system assembled. The loading structure is shown



(2018a). The coil-ends were preloaded by tensioning the rods to 70 MPa, corresponding to 20% of the Lorentz forces in the coil ends during powering. The total preload provided by the rods at cold corresponds to 60% of the Lorentz forces.

In FRESCA2a, after the first loading step, a relative lateral shift of the coils of about 0.2 mm, caused by a misaligned coil pack, resulted in an unbalanced preload (a difference of 100 MPa in the two Ti posts). To compensate for this effect, an asymmetric loading was performed by removing 0.1 mm in the loading shims on both sides of coil CR1202. For FRESCA2b and FRESCA2c, the alignment procedure was improved using coil measuring machine (CMM) data, resulting in a well-balanced preload.

FRESCA2c was loaded for ultimate operation at 15 T, corresponding to 60 MPa in the shell, and 330 MPa in the post for CR1201 (CR1202 showing artificially higher stress for the reasons explained below). The rods were tensioned to 120 MPa, corresponding to 35% of the coil-end Lorentz forces at warm temperature and 70% at cold.

## 12.5 Magnet Tests

The FRESCA2 magnet was tested three times in the CERN magnet test facility: FRESCA2a in February 2017, FRESCA2b in August 2017, and FRESCA2c in May 2018. In addition to ramps to quench and the investigation of training performance, the test plans included ramp rate, protection studies, and magnetic measurements. The magnets were tested at both 1.9 K and 4.3 K, and thermal cycles were carried out to check quench memory. Quench locations were determined by analyzing signals recorded by voltage taps installed on the pole turns of each layer (10 per layer for a total of 40 voltage taps). The mechanical behavior was monitored by strain gauges mounted on the aluminum shell, the aluminum axial rods, and the poles of coils CR1201 and CR1202. We provide in this section a summary of the quench performance, the protection studies, and the magnetic and stress measurements.

### 12.5.1 Quench Performance

#### 12.5.1.1 First Assembly, FRESCA2a

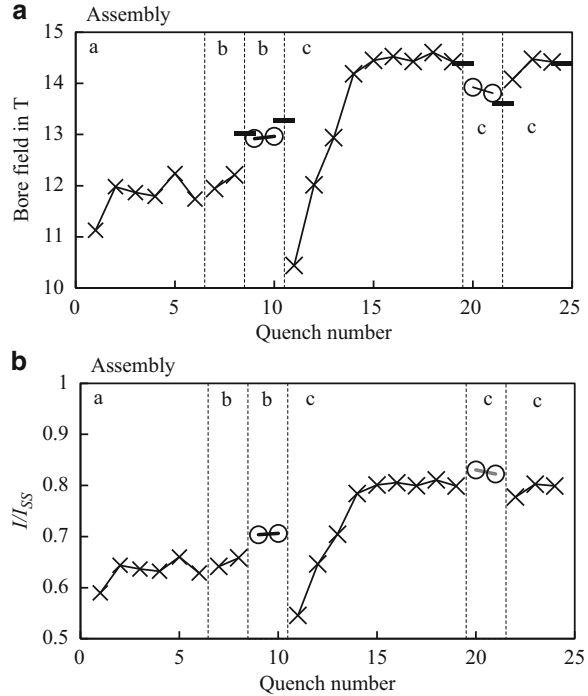
The tests were carried out as follows. The first protection studies were performed with quench heaters and energy extraction tests. Training to 13 T was then started at 1.9 K, followed by training at 4.2 K. Quench 1 of FRESCA2a was a typical pole turn quench, originating in the lower layer pole turn of coil CR1201, in the flared segment close to the head. Quenches 2–6 all originated due to the known cable damage in the splice region of coil CR3401 (described above). These quenches were reproducible, with the same pattern, same location, and same precursor. Therefore, one training quench can be considered for reaching 12.2 T in the first assembly (see Fig. 12.16).

The powering tests ended for FRESCA2a after quench 6, because during the discharge a quench heater of coil CR3401 failed, causing damage to the coil insulation.

#### 12.5.1.2 Second Assembly, FRESCA2b

The second assembly, FRESCA2b, reached its initial target field of 13 T after two quenches in the first cool-down at 1.9 K, see Fig. 12.16. The quenches occurred in

**Fig. 12.16** Training curves for FRESCA2a, b, and c: (a) bore field at quench current; (b) quench current normalized to the short sample. The marker crosses represent quench currents at 1.9 K, the round markers quench currents at 4.5 K, and the flat markers represent stable currents with no quench



the pole turn of coil CR1202 and in the second turn of coil CR1201, all in the high-field region in the straight section of the magnet.

Powering at 4.5 K resulted in two quenches just below 13 T. Both quenches occurred in the high-field region, in the straight segment of the pole turn of coil CR1202 and in the straight segment of the pole turn of coil CR1201. The number of training quenches up to 73% of the short sample limit is small compared to the predecessor magnets and model coils like HD and RMC.

A thermal cycle was performed, with the magnet reaching 280 K before cool-down to 1.9 K. After a thermal cycle the increased target field of 13.3 T was reached without quench.

All five recorded high-field quenches in the pole turns were preceded by rather large precursors in the voltages, indicating conductor movement as the cause of the quench. A detailed analysis of the test results can be found in Willering et al. (2018).

### 12.5.1.3 Third Assembly, FRESCA2c

A third assembly, FRESCA2c, has been prepared, with an increased preload for reaching the ultimate field of 15 T. The magnet reached a maximum record bore field of 14.6 T after seven additional quenches at 1.9 K. After a thermal cycle the magnet showed a good memory with only one retraining quench. Two stable currents at

14.4 T during 1 h were obtained at 1.9 K, and one stable current at 13.6 T during 1 h at 4.5 K. The magnet did not reach the conductor limit, but was limited by vibrations, in just one coil, indicating the potential for higher currents. The analysis of the tests is ongoing, and will be described in Willering et al. (n.d.).

## 12.5.2 Mechanical Analysis

### 12.5.2.1 Cool-Down

The data acquired during the different load-steps provided useful information for model tuning and FEM parameter validation. To better match the measurements with FEM simulations during the cool-down, 2D parametric studies for different material properties, contact conditions, and friction coefficients were performed. The cool-down is modeled with linear thermal contractions and homogeneous temperatures. The material properties are similar to the values proposed for MQXF magnets.

In particular, the contact conditions between the vertical pad, the iron post 3–4, and the Ti post 1–2 have a significant impact on the post stress. For FRESCA2a, the stress in the posts closely followed the simulated values. During the first cool-down of FRESCA2b, however, the contact conditions in coil CR1202 changed and a higher stress appeared in the post (see Fig. 12.17a). This behavior is attributed to a loss of contact at the top faces between Ti post 1–2 and iron post 3–4 (a detailed explanation can be found in Rochepault et al. (2018a)). The consequence is an additional bending stress, increasing the total stress measured in the post. Fortunately, an additional bending of the post has a marginal impact on the coil peak stress. The hypothesis of a lack of contact between the horizontal pad and coil 3–4, translating into a higher preload of coil 1–2, has been ruled out using stress-sensitive films during magnet assembly (Bourcey et al. 2018).

After warm-up, a loss of stress of about 20 MPa is observed in the Al shell. This effect is reproduced in the FEM by allowing a plasticization of the coil pack. According to the FEM, it is not attributed to friction.

### 12.5.2.2 Powering

As the coil is energized, the posts will be laterally un-loaded and the shell will be azimuthally stretched under the outward Lorentz forces. The post unloads linearly with the square of the current (with the first-order proportional to the Lorentz forces, see Fig. 12.17a). The measured slope is higher than predicted by the model, which could be due to changes in contact conditions, as suggested by Rochepault et al. (2018a).

Figure 12.17b shows the evolution of the shell azimuthal stress with the current squared. The measured data are compared with two 3D FEMs: the nominal model, assuming perfectly bonded contacts between the coils and posts; and a model considering sliding contact between the coils and the posts, with friction and

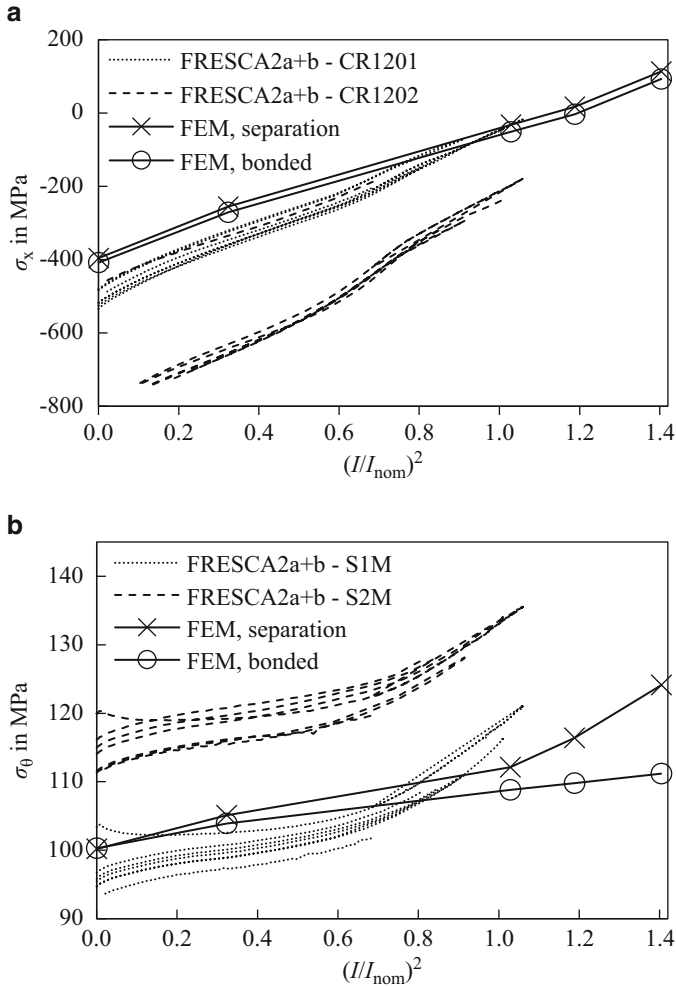


**Fig. 12.17** (a) Lateral post stress; and (b) azimuthal shell stress during powering as a function of the current squared. The data from FRESCA2a (last quench) and FRESCA2b (six current ramps) are compared with 3D finite element models using two different coil–post contact conditions (bonded and separation)

separation allowed. At low current, the azimuthal stress  $\sigma_\theta$  in the shell follows the model. The slope changes at  $(I/I_{nom})^2 = 0.6$ , so  $I = 8.2$  kA. This effect can be an indication of a de-bonding, after which the coil is pushing on the shell. This behavior is suggested by the 3D FEM, for which separation is allowed. This de-bonding, however, occurred at a lower current (8.2 kA) than predicted by the model (10.55 kA). This is currently unexplained, and could be attributed either to a loss of preload during cool-down, or additional magnetic forces between the iron parts. The impact of de-bonding on the pole stress is marginal.

Similarly, the axial rod stress is slightly increasing with the current squared, as predicted by the model. For FRESCA2c, the strain gauges show a similar behavior, except that the curves are shifted due to the higher preload. The change of slope occurs at a higher current and the poles remains in compression. The mechanical analysis is described in Willering et al. (n.d.).

### ***12.5.3 Magnetic Measurements***

The magnetic field of FRESCA2b has been measured with a cold rotating shaft with five coil segments, each 247 mm long. In Fig. 12.18, the measured data is compared with the bore field profile given by the 3D FEM, and the values averaged on the segments' length. The measurements confirm that the nominal field is reached with 13.04 T at 10.6 kA. The homogeneity of the magnetic field has been measured for the five middle segments of the magnetic measurement shaft. Figure 12.18 shows that the field profile is homogeneous within 1.5% over a length of 0.7 m, which is within the original 2% specification.

Field quality measurements have also been performed, and the field harmonics and transfer functions are within a few percent of the predictions (as shown in Figs. 12.19 and 12.20).

### ***12.5.4 Protection Studies***

#### **12.5.4.1 Quench Heaters**

In FRESCA2a, one heater strip failed at quench 6, with large damage of the coil-to-heater insulation, and the magnet test was not continued. In FRESCA2b, another strip failed during the first discharge, fortunately with less damage to the insulation, and the powering tests could continue. The failures have been linked to bad impregnation of the heater. It was decided to continue powering with protection from energy extraction alone.

#### **12.5.4.2 Energy Extraction**

For energy extraction, the test station is equipped with a thyristor switch that is allowed to switch in an extraction resistor with a delay of less than 4 ms after triggering. The maximum switching voltage of this switch is 1 kV, therefore a maximum extraction resistance of 80 m $\Omega$  was chosen (81 m $\Omega$  is considered when including the rest of the warm part of the circuit). The magnet protection was assessed by a series of energy extraction tests, where the energy extraction (in the dump resistor) was manually triggered and the current decay was analyzed, see

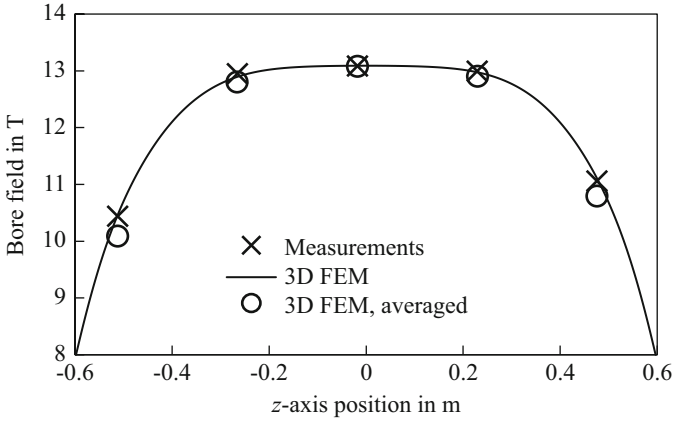


**Fig. 12.18** Average magnetic field measured in five 250 mm long segments (shown as crosses). The calculated field profile along the  $z$  axis is shown by the line

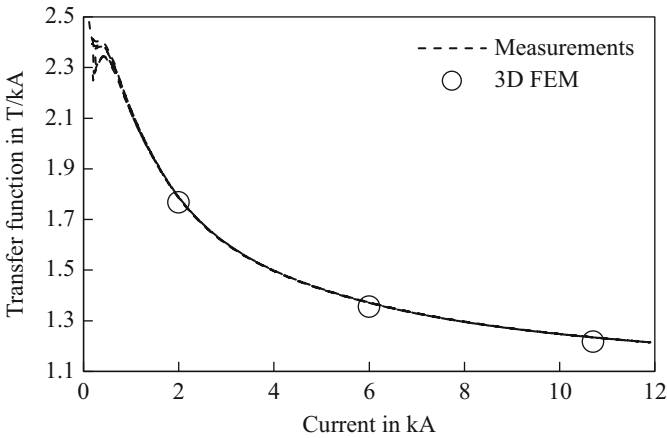


**Fig. 12.19** Measured and computed transfer functions at the central section of the magnet as a function of magnet current

Fig. 12.21. The measured quench integral ( $QI$ ) at 10.85 kA is 33.4 MA<sup>2</sup>s, corresponding to a hot-spot temperature of 157 K, which is a reduction of more than 30% compared to the calculated 48.3 MA<sup>2</sup>s, corresponding a hot-spot temperature of about 250 K. The difference can be entirely assigned to the effect of quench-back. The tests demonstrate that the contribution of the quench heaters to the reduction in  $QI$  was insignificant compared to the energy extraction and quench-back.

An effect of quench-back is a larger energy dissipation in the magnet and helium bath. At 10.85 kA about 30% of the magnet energy is dissipated in the magnet.

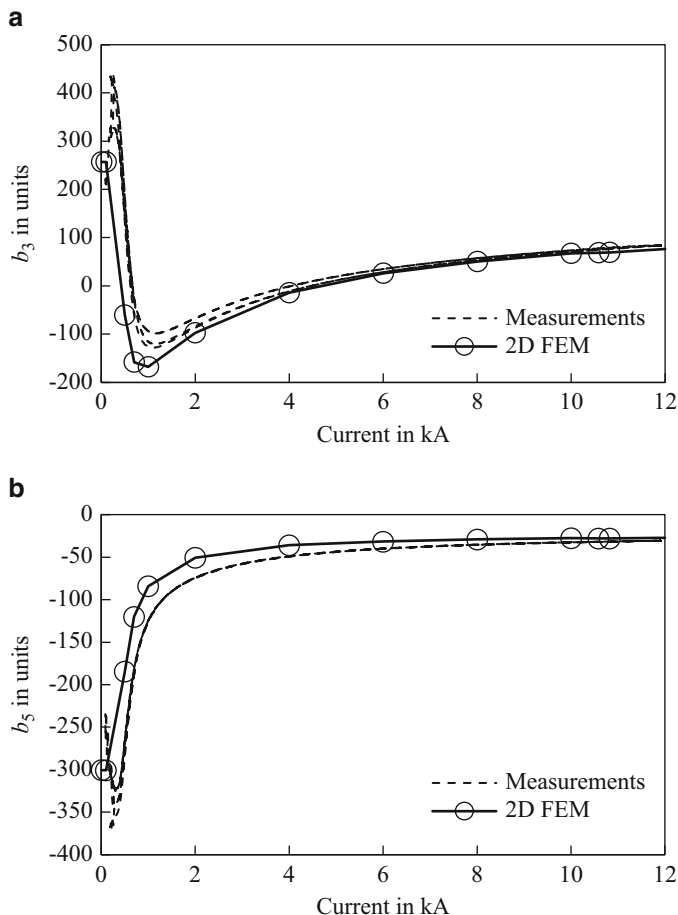


**Fig. 12.20** Measured and computed (a) sextupole  $b_3$ ; and (b) decapole  $b_5$  normalized harmonics at a reference radius of 33 mm for the central section of the magnet, as a function of magnet current

### 12.5.4.3 Protection Parameters and Hotspot Temperature

The electrical resistance of several high-field cable segments during current decay was measured, which allowed estimation of the local temperature. This estimate showed that the temperature in the high-field part of the coil did not exceed 100 K.

Based on the analysis of the time to rise to 100 mV for the five quenches in the high-field zone and the five quenches in the low-field zone, a threshold of 100 mV and a validation time of 10 ms are foreseen for operation. A variable threshold protection card should reduce the sensitivity to low-field flux jumps. Using these parameters, the maximum temperature that is expected to be reached in the magnet is about 160 K at 13 T and 180 K at 15 T.

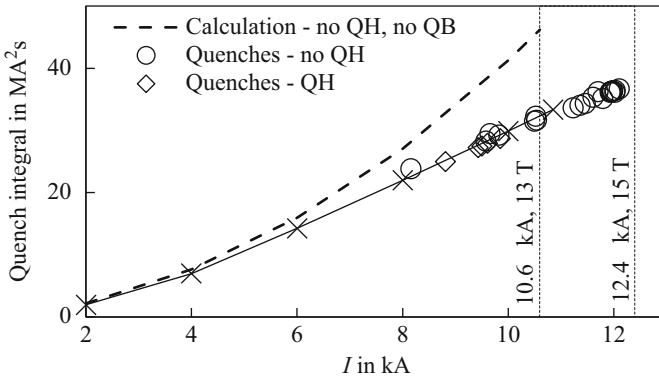


**Fig. 12.21** Quench integrals from the triggering of the quench protection at 1.9 K with and without quench heaters (QH) and the consideration of quench-back (QB)

## 12.6 Conclusions

The FRESCA2 project started in 2009, with the aim to design, fabricate, and test a 13 T Nb<sub>3</sub>Sn dipole for CERN's cable test facility. A block-coil layout with two double pancakes and flared ends was chosen, with a design inspired by the HD magnets. The structure is shell-based with a room-temperature preload using bladders and keys.

Six coils have been fabricated following different steps at CEA Saclay and at CERN. So far all tested coils have used RRP wire. One additional coil using PIT conductor is foreseen. The first magnet assembly, FRESCA2a, has been prepared and tested in liquid helium, reaching a maximum central field of 12.2 T. Unfortunately, coil CR3401 showed limitations during the tests because of fabrication issues, and was replaced with coil CR3403 in the second assembly FRESCA2b. The magnet reached a maximum bore field of 13.3 T in only three quenches, slightly above its nominal current. At 13 T the magnet showed stable operation for the 4 h test duration, which validates the powered performance of the magnet. Protection studies were performed, showing an important contribution of quench-back in the reduction of the quench integral at high current levels. During powering, the stress on the posts and the shell showed potential signs of coil–post detachment, at a current lower than the nominal. Even though there was no sign of premature quenches or degradation, it was decided not to power the magnet at higher currents. A final assembly, FRESCA2c, has been prepared, increasing the preload in order to reach a central field of 15 T. The magnet was able to reach a field record of 14.6 T after only seven additional quenches at 1.9 K. All magnet assemblies showed a negligible reduction of quench currents after a thermal cycle.

With this achievement, the FRESCA2 magnet demonstrated that the technology of block-coils with flared ends is able to reach fields close to 15 T in a rather large aperture. It confirms a great potential of this design for future 16 T accelerator dipoles.

In addition to a proof of concept of high-field Nb<sub>3</sub>Sn magnet technology, the FRESCA2 magnet, once installed in the test facility, is foreseen to be extensively used to test superconducting cables and HTS inserts in a large background field. Together with HTS inserts, magnetic fields of up to 20 T may be approached in FRESCA2 in a dipole configuration with apertures relevant for accelerators.

## References

- Bordini B, Bottura L, Mondonico G et al (2012) Extensive characterization of the 1 mm PIT Nb<sub>3</sub>Sn strand for the 13-T FRESCA2 magnet. *IEEE Trans Appl Supercond* 22(3):6000304. <https://doi.org/10.1109/tasc.2011.2178217>
- Bourcey N, Zurita AC, Durante M et al (2018) Assembly of the Nb<sub>3</sub>Sn dipole magnet FRESCA2. *IEEE Trans Appl Supercond* 28(3):4007505. <https://doi.org/10.1109/tasc.2018.2809703>
- de Rijk G (2012) The EuCARD high field magnet project. *IEEE Trans Appl Supercond* 22(3):4301204. <https://doi.org/10.1109/tasc.2011.2178220>
- Devaux-Bruchon M, Durante M, Karppinen M et al (2010) EuCARD-HFM dipole model design options. EuCARD-REP-2010-002, Oct. CERN, Geneva
- Devred A, Baudouy B, Baynham DE et al (2006) Overview and status of the next European dipole joint research activity. *Supercond Sci Technol* 19(3):S67–S83. <https://doi.org/10.1088/0953-2048/19/3/010>
- Devred A, Boutboul T, Oberli L (2007) Status of NED conductor development. *IEEE/CSC & ESAS European Superconductivity News Forum* no. 2, no. ST5, Oct
- Durante M, Garcia Fajardo L, Ferracin P et al (2016) Geometrical behavior of Nb<sub>3</sub>Sn Rutherford cables during heat treatment. *IEEE Trans Appl Supercond* 26(4):4802705. <https://doi.org/10.1109/TASC.2016.2530166>
- Durante M, Borgnolutti F, Bouziat D et al (2018) Realization and first tests of the EuCARD 5.4-T REBCO dipole magnet. *IEEE Trans Appl Supercond* 28(3):4203805. <https://doi.org/10.1109/TASC.2018.2796063>
- Felice H, Ambrosio G, Chlachidze G et al (2009) Instrumentation and quench protection for LARP Nb<sub>3</sub>Sn magnets. *IEEE Trans Appl Supercond* 19(3):2458–2461. <https://doi.org/10.1109/TASC.2009.2019062>
- Ferracin P, Devaux M, Durante M et al (2013) Development of the EuCARD Nb<sub>3</sub>Sn dipole magnet FRESCA2. *IEEE Trans Appl Supercond* 23(3):4002005. <https://doi.org/10.1109/TASC.2013.2243799>
- Leroy D, Spigo G, Verweij AP et al (2000) Design and manufacture of the large-bore 10 T superconducting dipole for the CERN cable test facility. *IEEE Trans Appl Supercond* 10(1):178–182. <https://doi.org/10.1109/77.828205>
- Lorin C, Durante M, Fazilleau P et al (2016) Development of a Roebel-cable-based cos-theta dipole: design and windability of magnet ends. *IEEE Trans Appl Supercond* 26(3):4003105. <https://doi.org/10.1109/TASC.2016.2528542>
- Manil P (2013) Design report for the dipole magnet (Part I). In: Bajas H, Baudouy B, Benda V et al (eds) Dipole model test with one superconduction coil; results analysed. Deliverable: D7.3.1 EuCARD-REP-2010-013, June. CERN, Geneva
- Manil P, Baudouy B, Clement S et al (2014) Development and coil fabrication test of the Nb<sub>3</sub>Sn dipole magnet FRESCA2. *IEEE Trans Appl Supercond* 24(3):4001705. <https://doi.org/10.1109/TASC.2013.2285879>
- Milanese A, Devaux M, Durante M et al (2012) Design of the EuCARD high field model dipole magnet FRESCA2. *IEEE Trans Appl Supercond* 22(3):4002604. <https://doi.org/10.1109/TASC.2011.2178980>

- Oberli L (2013) Development of the Nb<sub>3</sub>Sn Rutherford cable for the EuCARD high field dipole magnet FRESA2. *IEEE Trans Appl Supercond* 23(3):4800704. <https://doi.org/10.1109/TASC.2012.2236602>
- Perez JC, Bajko M, Bajas H et al (2015) Performance of the short model coils wound with the CERN 11-T Nb<sub>3</sub>Sn conductor. *IEEE Trans Appl Supercond* 25(3):4002805. <https://doi.org/10.1109/TASC.2014.2381364>
- Perez JC, Bajas H, Bajko M et al (2016) 16 T Nb<sub>3</sub>Sn racetrack model coil test result. *IEEE Trans Appl Supercond* 26(4):4004906. <https://doi.org/10.1109/TASC.2016.2530684>
- Rochepault E, Ferracin P, Ambrosio G et al (2016) Dimensional changes of Nb<sub>3</sub>Sn Rutherford cables during heat treatment. *IEEE Trans Appl Supercond* 26(4):4802605. <https://doi.org/10.1109/TASC.2016.2539156>
- Rochepault E, Bourcey N, Ferracin P et al (2017) Fabrication and assembly of the Nb<sub>3</sub>Sn dipole magnet FRESA2. *IEEE Trans Appl Supercond* 27(4):9500205. <https://doi.org/10.1109/TASC.2016.2636145>
- Rochepault E, Bourcey N, Ferracin P et al (2018a) Mechanical analysis of the FRESA2 dipole during preload, cool-down and powering. *IEEE Trans Appl Supercond* 28(3):4002905. <https://doi.org/10.1109/TASC.2017.2781704>
- Rochepault E, Izquierdo Bermudez S, Perez JC et al (2018b) 3D magnetic and mechanical design of coil ends for the racetrack model magnet RMM. *IEEE Trans Appl Supercond* 28(3):4006105
- Rondeaux F, Ferracin P, Durante M et al (2016) “Block-type” coils fabrication procedure for the Nb<sub>3</sub>Sn dipole magnet FRESA2. *IEEE Trans Appl Supercond* 26(4):4002405. <https://doi.org/10.1109/TASC.2016.2528049>
- Taylor C, Scanlan R, Peters C et al (1985) A Nb<sub>3</sub>Sn dipole magnet reacted after winding. *IEEE Trans Magn MAG* 21(2):967–970. <https://doi.org/10.1109/TMAG.1985.1063680>
- van Nugteren J, Kirby G, Bajas H et al (2018) Powering of an HTS dipole insert-magnet operated standalone in helium gas between 5 and 85 K. *Supercond Sci Technol* 31(6):065002. <https://doi.org/10.1088/1361-6668/aab887>
- Willering G, Petrone C, Bajko M et al (2018) Cold powering tests and protection studies of the FRESA2 100 mm bore Nb<sub>3</sub>Sn block-coil magnet. *IEEE Trans Appl Supercond* 28(3):4005105. <https://doi.org/10.1109/TASC.2018.2797907>
- Willering G, Bajko M, Bajas H et al (n.d.) Performance update of the FRESA2 100mm bore Nb<sub>3</sub>Sn block coil magnet. *IEEE Trans Appl Supercond* submitted

**Open Access** This chapter is licensed under the terms of the Creative Commons Attribution 4.0 International License (<http://creativecommons.org/licenses/by/4.0/>), which permits use, sharing, adaptation, distribution and reproduction in any medium or format, as long as you give appropriate credit to the original author(s) and the source, provide a link to the Creative Commons licence and indicate if changes were made.

The images or other third party material in this chapter are included in the chapter’s Creative Commons licence, unless indicated otherwise in a credit line to the material. If material is not included in the chapter’s Creative Commons licence and your intended use is not permitted by statutory regulation or exceeds the permitted use, you will need to obtain permission directly from the copyright holder.

